

Article

# Efficient Global Aerodynamic Shape Optimization of a Full Aircraft Configuration Considering Trimming

Kai Wang<sup>1,2</sup>, Zhonghua Han<sup>1,2,\*</sup>, Keshi Zhang<sup>1,2,\*</sup> and Wenping Song<sup>1,2</sup>

<sup>1</sup> National Key Laboratory of Science and Technology on Aerodynamic Design and Research, Xi'an 710072, China; wangkai450707@126.com (K.W.); wpsong@nwpu.edu.cn (W.S.)

<sup>2</sup> Institute of Aerodynamic and Multidisciplinary Design Optimization, School of Aeronautics, Northwestern Polytechnical University, Xi'an 710072, China

\* Correspondence: hanzh@nwpu.edu.cn (Z.H.); zhangkeshi@nwpu.edu.cn (K.Z.)

**Abstract:** Most existing aerodynamic shape optimization (ASO) studies do not take the balanced pitching moment into account and thus the optimized configuration has to be trimmed to ensure zero pitching moment, which causes additional drag and reduces the benefit of ASO remarkably. This article proposes an efficient global ASO method that directly enforces a zero pitching moment constraint. A free-form deformation (FFD) parameterization combining Laplacian smoothing method is implemented to parameterize a full aircraft configuration and ensure sufficiently smooth aerodynamic shapes. Reynolds-averaged Navier–Stokes (RANS) equations are solved to simulate transonic viscous flows. A surrogate-based multi-round optimization strategy is used to drive ASO towards the global optimum. To verify the effectiveness of the proposed method, we adopt two design optimization strategies for the NASA Common Research Model (CRM) wing–body–tail configuration. The first strategy is to optimize the configuration without considering balance of pitching moment, and then manually trim the optimized configuration by deflecting the horizontal tail. The second one is to directly enforce the zero pitching moment constraint in the optimization model and take the deflection angle of the horizontal tail as an additional design variable. Results show that: (1) for the first strategy, about 4-count drag-reducing benefits would be lost when manually trimming the optimal configuration; (2) the second strategy can achieve 3.2-count more drag-reducing benefits than the first strategy; (3) compared with gradient-based optimization (GBO), surrogate-based optimization (SBO) is more efficient than GBO for ASO problems with around 80 design variables, and the benefit of ASO achieved by SBO is comparable to that obtained by GBO.

**Keywords:** aerodynamic shape optimization; efficient global optimization; surrogate model; aircraft design; computational fluid dynamics



**Citation:** Wang, K.; Han, Z.; Zhang, K.; Song, W. Efficient Global Aerodynamic Shape Optimization of a Full Aircraft Configuration Considering Trimming. *Aerospace* **2023**, *10*, 734. <https://doi.org/10.3390/aerospace10080734>

Academic Editor: Lance Traub

Received: 19 July 2023

Revised: 16 August 2023

Accepted: 19 August 2023

Published: 21 August 2023



**Copyright:** © 2023 by the authors. Licensee MDPI, Basel, Switzerland. This article is an open access article distributed under the terms and conditions of the Creative Commons Attribution (CC BY) license (<https://creativecommons.org/licenses/by/4.0/>).

## 1. Introduction

Following the continuous advancement of computer performance and numerical computation methods, computational fluid dynamics (CFD) has been developed to an extent that it has become an important tool to predict the aerodynamic performance of a full aircraft configuration and replace expensive wind tunnel experiments partially. As a result, CFD-driven aerodynamic shape optimization (ASO) has partly replaced the traditional “cut and try” method and inverse design method, and is becoming the important way to improve the aerodynamic performance of an aircraft. However, it is still difficult to perform ASO of complex aircraft configurations such as the wing–body–tail configuration, since high-fidelity CFD simulation methods such as the Reynolds-averaged Navier–Stokes (RANS) equations are computationally expensive, and a large number of design variables and constraints can cause the optimization algorithm to suffer from numerical difficulties.

Surrogate-based optimization (SBO) has become one of the most attractive methods for ASO with high-fidelity flow simulations. The solution of expensive cost functions can be approximated by cheap-to-evaluate surrogate models to drive the addition and evaluation of

new sample point(s) towards the global optimum [1–3]. SBO requires much less expensive function evaluations to reach the global optimum compared with a genetic algorithm (GA), especially when expensive high-fidelity CFD is employed [4,5]. It is free of gradient information and can be used to solve problems with highly nonlinear and multi-modal design space [6–8]. Therefore, SBO has gained much attention in the area of engineering design optimization. Despite the popularity of SBO, it is still suffering from the difficulty associated with the “curse of dimensionality”, which means that the computational cost grows exponentially as the number of design variables increases. To improve the SBO efficiency, some advanced technologies have been proposed, such as evaluating the responses of the samples in parallel [9], variable-fidelity surrogate modeling [10–16], surrogate modeling incorporating cheap gradients [17–20], deep-learning-based optimal sampling [21], and applying dimension reduction [22,23] and constraint aggregation during optimization [24,25].

However, the design optimization of complex aircraft configurations such as the wing–body–tail configuration brings a large challenge to SBO. First, both design of experiment (DoE) and sub-optimization within the framework of SBO are pure numerical methods designed to generate samples without considering feasibility. Thus, many samples associated with unsmooth aerodynamic shapes would be generated via DoE and sub-optimization during optimization, which results in an unpractical optimal aerodynamic shape [22]. Second, the size of the design space directly affects the optimization results, and an inappropriate design space makes it difficult for SBO to obtain the global optimal solution [26,27]. Third, although fast design can be achieved by using a low-fidelity CFD solver in the optimization, the benefit of drag reduction cannot be realized completely when verifying the optimal solution by the high-fidelity CFD simulation such as solving the RANS equations [28]. Finally, it is unsuitable to design the wing of a complex aircraft configuration only since the benefit of drag reduction achieved would decrease significantly due to the trim drag induced by trimming the full aircraft configuration [29]. Recently, some design works considering trimming have been performed via the gradient-based optimization (GBO) [30–34]; however, the adjoint equations for solving the derivatives of the added constraints, such as the zero pitching moment constraint, must be derived, and solving the added adjoint equations can be expected to increase the computational cost of GBO significantly.

This article aims to propose an efficient global ASO method using surrogate models to design complex aircraft configurations, in which trimming is considered by adding a zero pitching moment constraint during optimization. The multi-round optimization strategy is used to drive SBO towards the global optimum by adjusting the design space in each round according to the optimum from the previous round. The Laplacian smoothing method is conducted to avoid obtaining unsmooth optimal aerodynamic shapes. To validate the proposed method, two optimization strategies are applied to design the NASA CRM wing–body–tail configuration. The first strategy is to optimize the wing only and then manually trim the optimal configuration by deflecting the horizontal tail as a solid body. The second strategy is to consider trimming during optimization. Then, all optimization results obtained via SBO are compared with those obtained via GBO. Two goals are involved in this work; one is to validate SBO for solving ASO of a complex aircraft configuration, since there is hardly any research focus on high-fidelity surrogate-based ASO of such a complex aircraft configuration. The other one is to compare the optimization results achieved through different optimization strategies, thus providing some useful guidance for future work.

This article proceeds with Section 2, where the numerical tools employed in this study are described. Section 3 illustrates the problem formulation, while Section 4 presents ASO of the NASA CRM wing–body–tail configuration and corresponding results. In Section 5, conclusions are presented.

## 2. Methodology

### 2.1. Geometric Parametrization

The free-form deformation (FFD) method [35] based on the non-uniform rational B-spline (NURBS) is applied to parametrize the NASA CRM wing–body–tail configuration, which can change the geometry by perturbing the FFD control point. As shown in Figure 1, the FFD volume has a total of 25 FFD volumetric blocks, one FFD volumetric block with 90 control points is used to parametrize the wing, and another one with 66 control points is used to parametrize the horizontal tail.

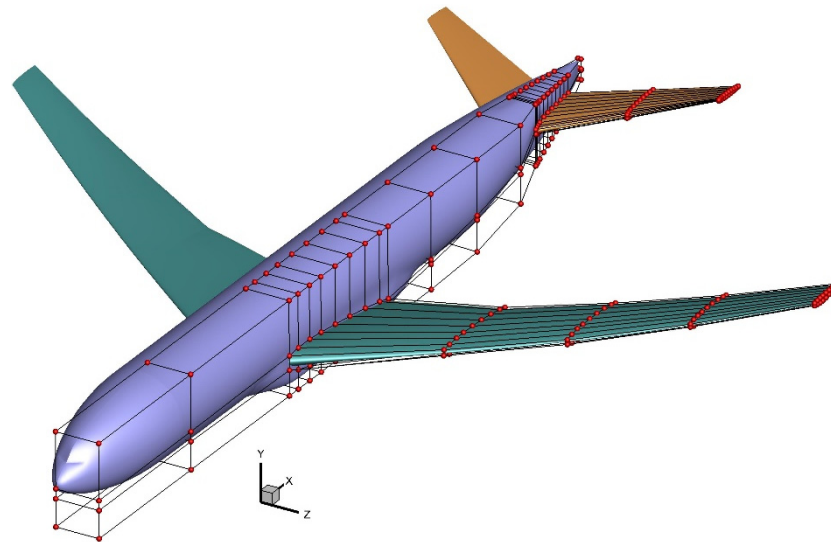


**Figure 1.** FFD parameterization for the NASA CRM wing–body–tail configuration.

### 2.2. Laplacian Smoothing of Aerodynamic Shape

In a typical progression of surrogate-based ASO, a DoE method such as Latin hypercube sampling (LHS) [36] is used to generate initial sample points, and the sub-optimization defined by a certain infill-sampling criteria is used to select new samples in each SBO iteration. However, both DoE and sub-optimization are pure numerical methods designed to generate samples without considering feasibility. As a result, an increasing number of samples associated with unsmooth aerodynamic shapes are generated during optimization, which results in an unpractical optimal aerodynamic shape.

To address this issue, the Laplacian smoothing method is introduced in SBO to smooth the aerodynamic shapes corresponding to the samples generated by DoE and sub-optimization. The Laplacian smoothing method is defined as

$$y^i = \theta y^i + \frac{1 - \theta}{n_{neighbor}} \sum_{j=1}^{n_{neighbor}} y^j, \quad (1)$$

where  $y^i$  denotes the  $y$ -direction deformation of the  $i$ -th FFD control point used to parametrize the wing and where  $\theta$  is used as a weight coefficient, which can influence the smoothing operation speed. Li et al. found that a practical aerodynamic shape can be obtained via an efficient smoothing operation when  $\theta = 0.5$  [22]. Therefore,  $\theta$  is set as 0.5 in this article. In addition,  $n_{neighbor}$  denotes the number of FFD control points adjacent to the  $i$ -th control point, and it is set as 4 for our studies.

The pseudo code of the Laplacian smoothing method is given in Algorithm 1, which describes the smoothing progress in detail. As shown in Figure 2, the aerodynamic shape of a typical sample obtained randomly via DoE is smoothed by using the Laplacian smoothing method, resulting in a smooth and practical aerodynamic shape.

**Algorithm 1** Laplacian smoothing algorithm

```

Input  $y_{initial}$  /*initial y-axis direction deformations of FFD control point*/
Output  $y_{smoothing}$  /*y-axis direction deformations of FFD control points obtained via Laplacian smoothing*/
Procedure Smoothing ( $y_{initial}$ )
 $y_{smoothing} = y_{initial}$ 
 $\epsilon_g = 0.035$  /*convergence criterion is set as 0.035*/
 $\epsilon_g = 0$ 
 $V_{smoothing} = FED(y_{initial})$ 
/* perform FFD parameterization and get initial y - axis deirection coordinates of the wing surface mesh */
while  $\epsilon < \epsilon_g$  do
  for each FFD control point i do
     $y_{smoothing}^i = \theta y_{smoothing}^i + \frac{1-\theta}{n_{neighbor}} \sum_{j=1}^{n_{neighbor}} y_{smoothing}^j$  /*Laplacian smoothing function */
  /*  $\theta = 0.5$  in this article,  $n_{neighbor} = 4$  for the wing*/
  end for
   $V_{smoothing} = FFD(y_{smoothing})$  /*update the y - axis direction coordinates of the wing surface mesh */
   $\epsilon = \frac{\|V_{smoothing} - V_{initial}\|}{\|V_{initial}\|}$  /* calculate the relative error */
end while
end Procedure
    
```

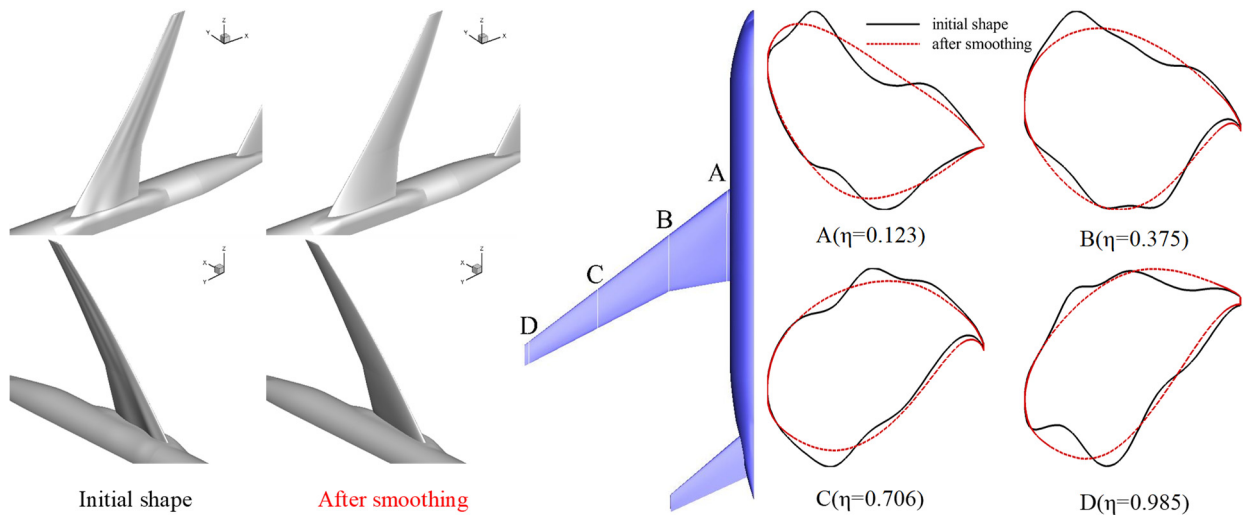


**Figure 2.** Comparison of wing–body–tail configurations before and after Laplacian smoothing.

2.3. Flow Solver

We use the open-source code “Adflow” as the flow solver [37]. It is a finite-volume, cell-centered multi-block solver for RANS equations, and can be employed to calculate the gradients required for the optimizations by using the discrete adjoint method.

2.3.1. Governing Equation of Flow and Discretization Scheme

For the control volume  $V$  and surface element  $dS$ , Navier–Stokes equations in integral form can be defined as

$$\iiint_{\Omega} \frac{\partial Q}{\partial t} dV + \iint_{\partial\Omega} \mathbf{F} \bullet \mathbf{n} dS = \iint_{\partial\Omega} \mathbf{F}_v \bullet \mathbf{n} dS, \tag{2}$$

where  $Q = [\rho, \rho u, \rho v, \rho w, \rho E]^T$  denotes the conservation variables.  $\partial\Omega$  denotes the control volume boundary,  $\mathbf{n}$  is the surface normal of  $\partial\Omega$ .  $\mathbf{q} = (u, v, w)^T$  is the Cartesian velocity

vector.  $\rho$  is the density.  $E$  is the specific total energy.  $F, F_v$  denote the inviscid and viscous flux vector, respectively.

The Jameson–Schmidt–Turkel (JST) scheme with second-order accuracy [38] is used for the spatial discretization. The spatial discretization of Equation (2) for each grid cell  $i$  can be expressed as

$$\frac{\partial(Q_i V_i)}{\partial t} + \bar{R}_i = 0, \quad (3)$$

where  $V_i$  is the volume of current grid cell  $i$ .  $\bar{R}_i = R_i^c - R_i^v - D_i$  is the total residual of Equation (3),  $R_i, R_i^v$  denote the residual of the inviscid and the viscous flux respectively, and  $D_i$  is the artificial dissipation term added to prevent non-physical oscillations.

The first-order backward difference is performed on the time derivative term, Equation (3) can be written into the following implicit form

$$\frac{V_i(Q_i^{k+1} - Q_i^k)}{\Delta t} + \bar{R}_i^{k+1} = 0, \quad (4)$$

where  $\bar{R}_i^{k+1}$  can be written as

$$\bar{R}_i^{k+1} = R_i^{c,k+1} - R_i^{v,k} - D_i^k, \quad (5)$$

where the superscript  $k$  represents the number of the time step. The diagonally dominant alternating direction implicit (DD-ADI) method [39] is employed for the implicit solution. Furthermore, the Spalart–Allmaras (SA) one-equation turbulence model is used to compute turbulence viscosity coefficient.

### 2.3.2. Discrete Adjoint Method

For ASO problems, derivatives of the cost functions  $F$  with respect to the design variables  $x$  can be obtained by

$$\frac{dF}{dx} = \frac{\partial F}{\partial x} + \psi^T \frac{\partial R}{\partial x}, \quad (6)$$

where  $\psi$  denotes the adjoint variables, and  $\partial R / \partial x$  represents partial derivatives of the residual of the governing equations with respect to the design variables.  $\psi$  can be achieved by solving adjoint equations.

$$\left[ \frac{\partial R}{\partial w} \right]^T \psi = \left[ \frac{\partial F}{\partial w} \right]^T, \quad (7)$$

where  $w$  denotes flowfield variables, such as  $\rho$  and  $u, v, w$ . The preconditioned generalized minimal residual (GMRES) [40] solver from PETSc [41] is used for solving the adjoint equations.

### 2.4. Mesh Perturbation Method

Since the deformations of the FFD control volumes can change the embedded geometry during optimization, an in-house mesh perturbation code “GridDeform” is used to perturb the CFD mesh according to the new geometry. The core idea of the mesh perturbation method used in this article is to interpolate the deformation of the surface mesh to the far field by using the radial basis function (RBF). In addition, the Intel Math Kernel Library (MKL) is used to solve large linear systems under the parallel computing environment, which makes the in-house mesh perturbation code capable of perturbing the CFD mesh with large-scale cells efficiently in parallel.

### 2.5. SBO Algorithm

To find the global optimum, a surrogate-based multi-round optimization strategy is introduced into our study. The main loop of this method is shown in Figure 3. Its core idea

is to adjust the design space in each round according to the optimal aerodynamic shape obtained from the previous round.

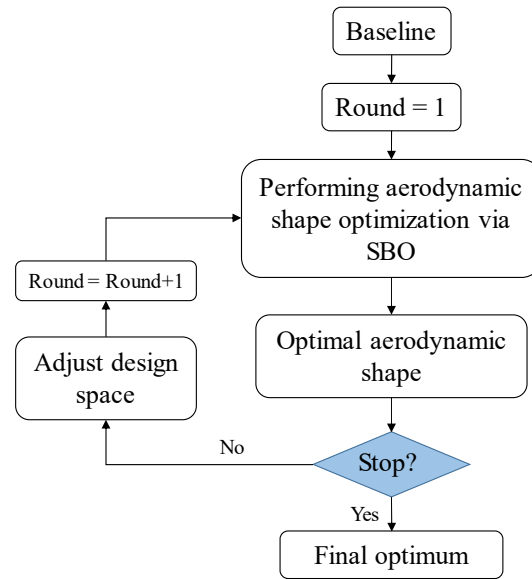


Figure 3. Flowchart of multi-round optimization strategy.

The in-house SBO code “SurroOpt” [8,42–44] is used in our studies. Figure 4 sketches the optimization framework of SurroOpt. The optimization progress can be described as

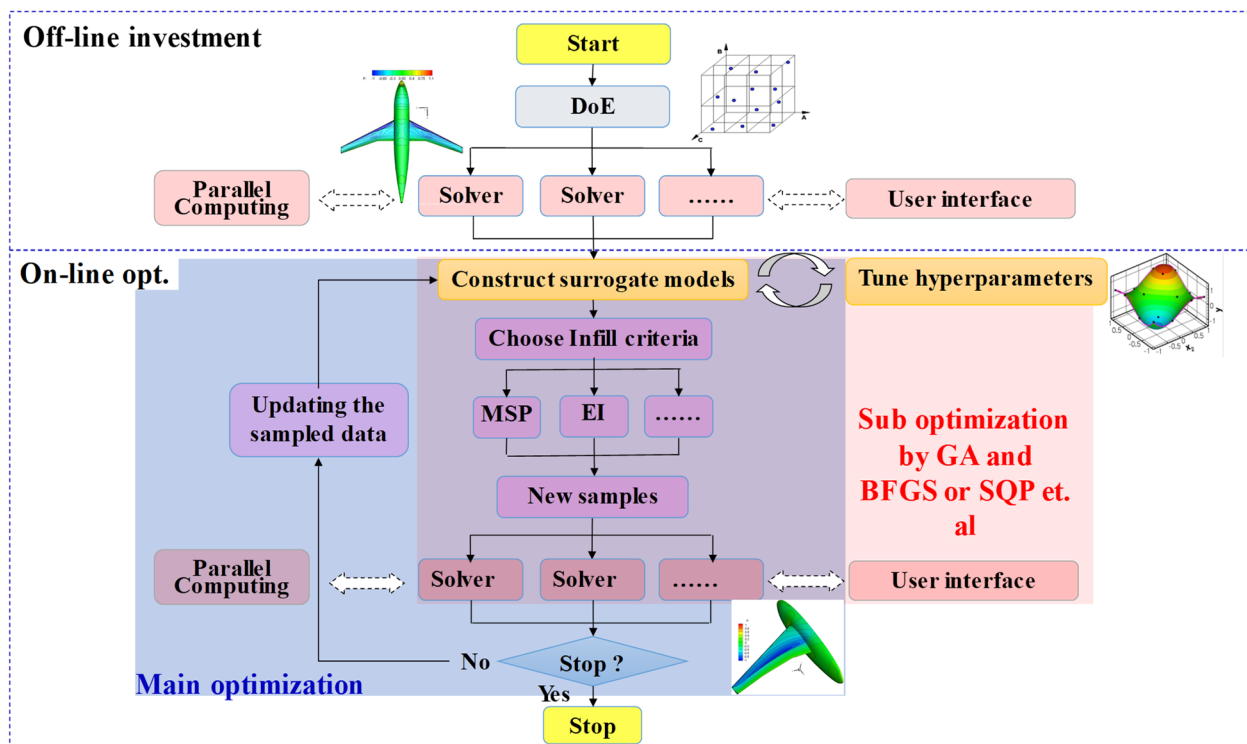


Figure 4. Framework of SurroOpt [8,42–44].

- (1) LHS is selected to generate 100 initial samples. Then, the aerodynamic shapes generated by these samples are smoothed by using the Laplacian smoothing method, and corresponding responses are solved by Adflow;
- (2) Initial kriging models are built based on the samples and corresponding responses;

- (3) The parallel infill-sampling criteria, combining the expected improvement (EI) and minimizing surrogate prediction (MSP), are used to generate two new samples. The new aerodynamic shapes are smoothed by using the Laplacian smoothing method, and corresponding responses are solved by Adflow;
- (4) Kriging models are updated based on these smoothed samples and their responses.
- (5) Steps 3 and 4 are repeated until one of the termination conditions is satisfied.

### 3. Problem Formulation

#### 3.1. Baseline Geometry

The NASA CRM wing–body–tail configuration is treated as the baseline geometry, as shown in Figure 5. The reference point is located at 25% of mean aerodynamic chord. The nose is located at the origin of coordinates and the span-wise direction is set parallel to the z-axis direction. The reference point is located at  $(x, y, z) = (31.32972, -0.50934, 0.007669)$  m. The reference length is 7.00532 m, and the reference area is 191.8448 m<sup>2</sup>.

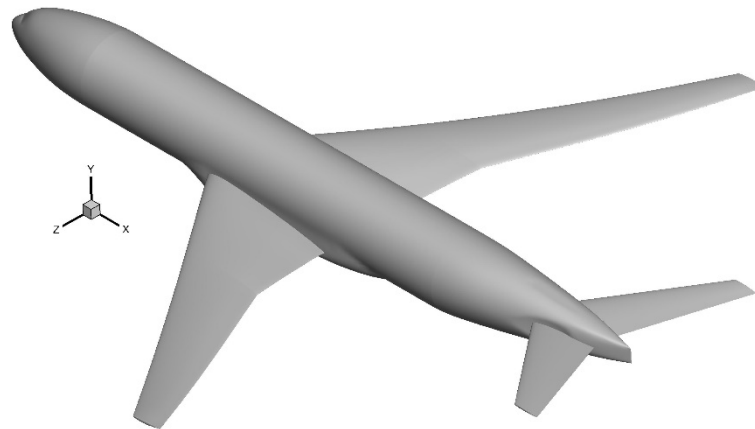


**Figure 5.** NASA CRM wing–body–tail configuration.

#### 3.2. Mesh Convergence Study

Three coarsening levels of multi-block CFD structured grids are generated by ANSYS ICEM CFD and shown in Figure 6. L2, L1, and L0 represent the coarse grid, medium grid, and fine grid, respectively, and each grid has 273 blocks. The first cell height  $\Delta_1$ , mesh size, and  $y^+$  values are listed in Table 1. A grid convergence study is performed based on these meshes. The flow condition is the lift coefficient  $C_L = 0.5$ , the freestream Mach number  $Ma = 0.85$ , and the Reynolds number  $Re = 5 \times 10^6$ . In addition, the drag coefficient  $C_D$  of the infinite-cell-grid is evaluated via Richardson extrapolation.

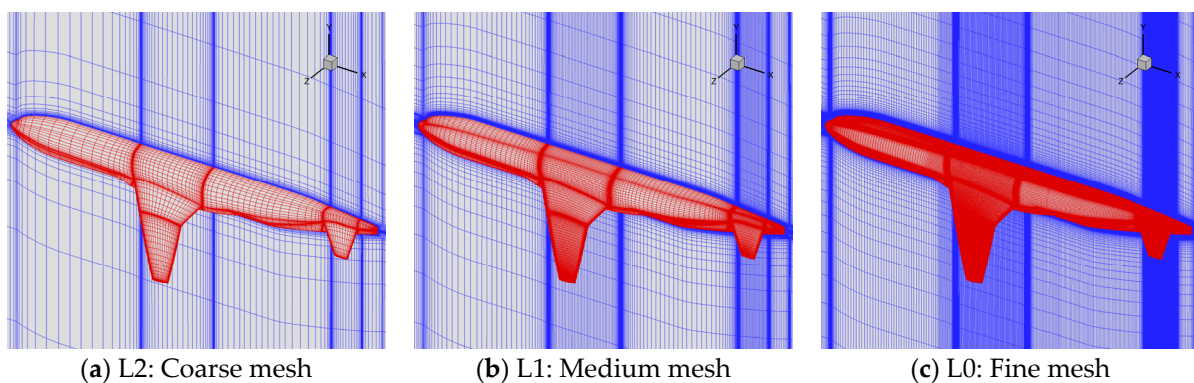


**Figure 6.** O-H multiblock structured meshes for the mesh convergence study.

**Table 1.** Details of baseline CFD grids.

Number	$\Delta_1$	$Y^+$	Number of Cells (Million)
L2	$3.69 \times 10^{-5}$	1.0	0.887
L1	$2.46 \times 10^{-5}$	2/3	6.776
L0	$1.64 \times 10^{-5}$	4/9	59.355

Table 2 lists the CFD simulation results of the baseline meshes. It is obvious that the drag coefficient of the baseline geometry decreases with increasing mesh size, while the moment coefficient increases. The same trend can be seen in Figure 7, which shows the drag and moment convergence plots with respect to  $1/\text{MeshSize}^{2/3}$ . The drag coefficient of the L0 grid is only 1.6 counts more than the zero grid spacing drag, which proves that the accuracy of the L0 mesh is close to the infinite-cell-grid.

**Table 2.** CFD simulation results of the mesh convergence study.

Mesh Levels	$C_L$	$C_D$	$C_{MZ}$
L00	0.5	0.02720	/
L0	0.5	0.02736	−0.0422
L1	0.5	0.02838	−0.0463
L2	0.5	0.03351	−0.0640

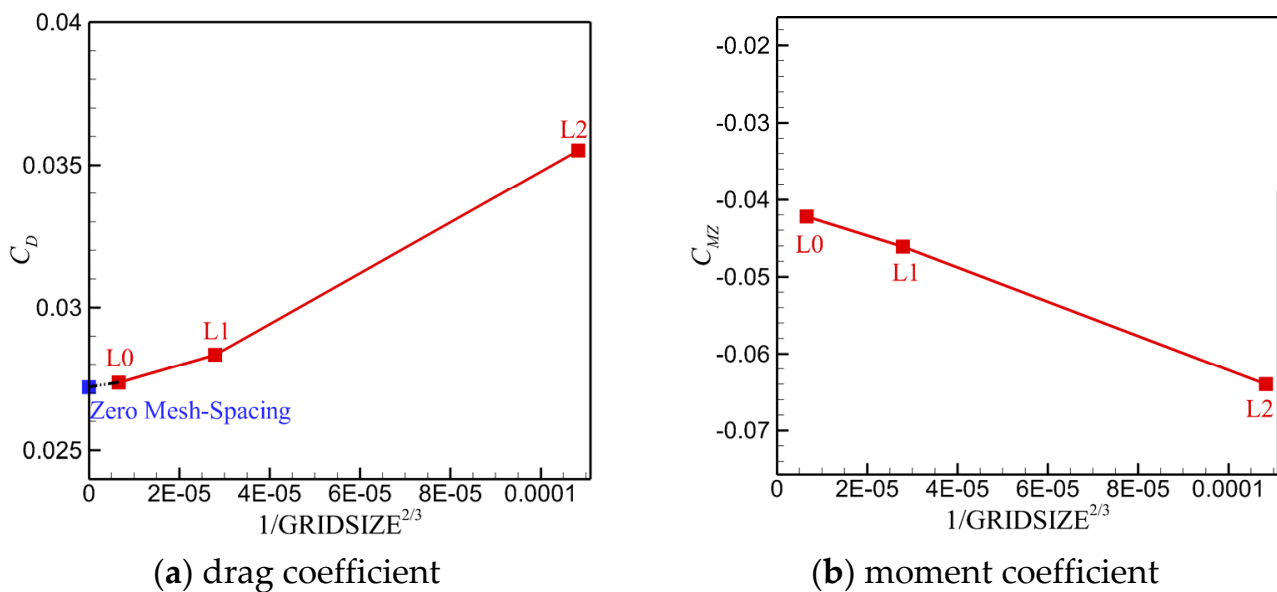
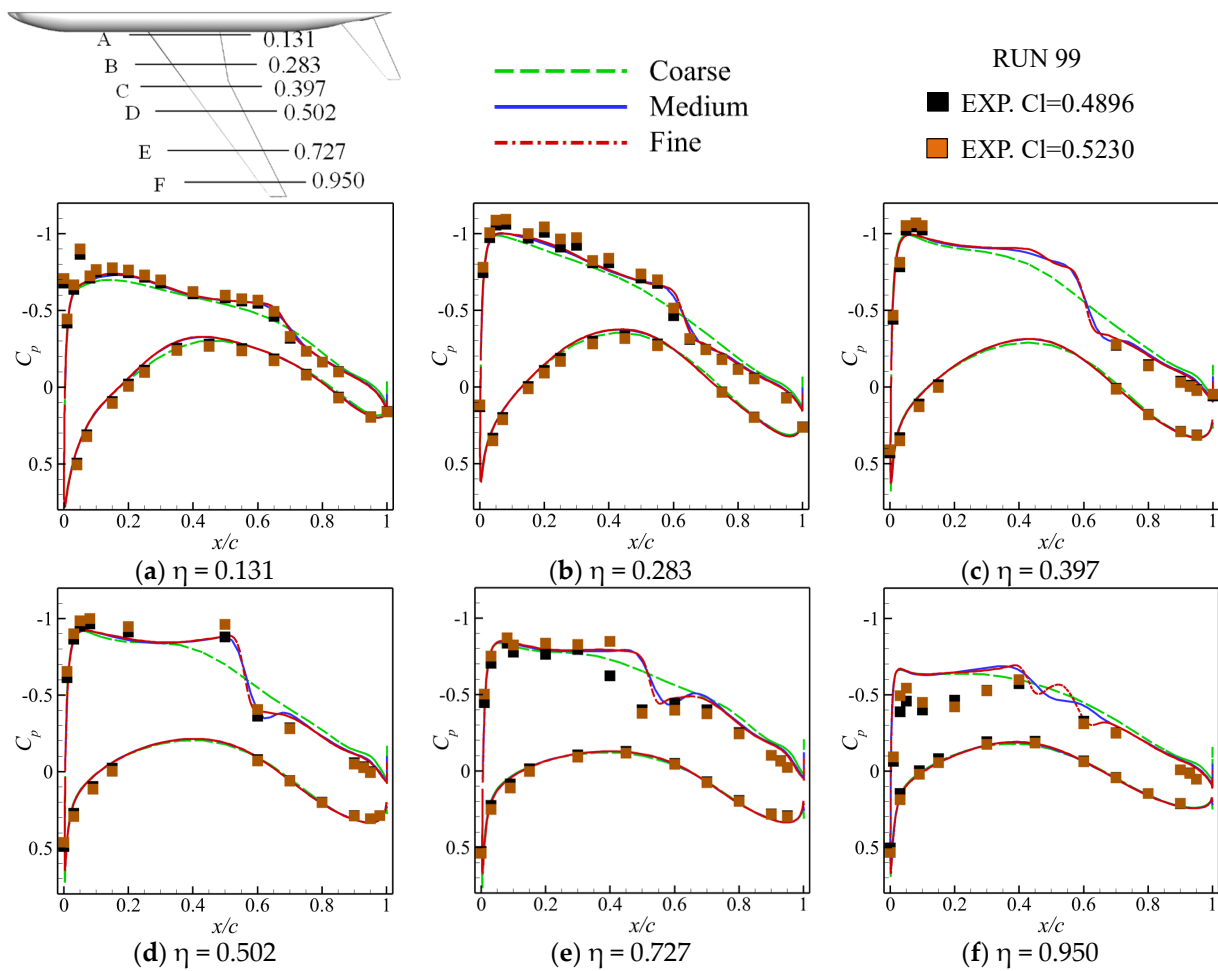
**Figure 7.** Mesh convergence for drag and moment coefficients of the baseline geometry.

Figure 8 compares sectional pressure distributions from the CFD simulation results with the experimental data from the National Transonic Facility (NTF) test. We can see that the CFD results get closer to the experimental data with increasing mesh size, and the L1 and L0 grids have sufficient accuracy. After considering the trade-off between computational time and accuracy, L1 mesh is applied to optimizations.



**Figure 8.** Comparison of sectional pressure distributions of the baseline geometry.

### 3.3. Optimization Problem Formulation

To ensure the lift constraint  $C_L = 0.5$  is satisfied, the angle of attack is treated as a design variable. As shown in Figure 1, the wing FFD volumetric block has a total of 90 control points. To fix the leading and trailing edge of the wing, the two control points at these locations of each control section share one design variable to move the same distance along the opposite directions. We also choose the y-axis direction displacements of the other 70 control points as design variables. Therefore, there are 80 wing shape variables in total.

To ensure that a practical design can be obtained, a volume constraint and a large number of thickness constraints are added to the optimization. The volume is enforced to be no less than that of the baseline wing. As shown in Figure 9, we impose 525 thickness constraints on the wing with 25 spanwise and 21 chordwise locations. These thicknesses are enforced to be no less than 85% of those of the baseline wing. To handle so many geometric constraints efficiently, the constant-parameter Kreisselmeier–Steinhauser (KS) method [45] is adopted to lump all the thickness constraints into one during optimization. Thus, the cost of optimization is greatly reduced. The KS method can be defined as

$$KS[g(x)] = g_{\max}(x) + \frac{1}{\rho_{ks}} \ln \left[ \sum_{j=1}^n e^{\rho(g_j(x) - g_{\max}(x))} \right] \quad (8)$$

where  $g_{\max}(x)$  denotes the maximum constraint value, and  $\rho_{ks}$  is the aggregation parameter.

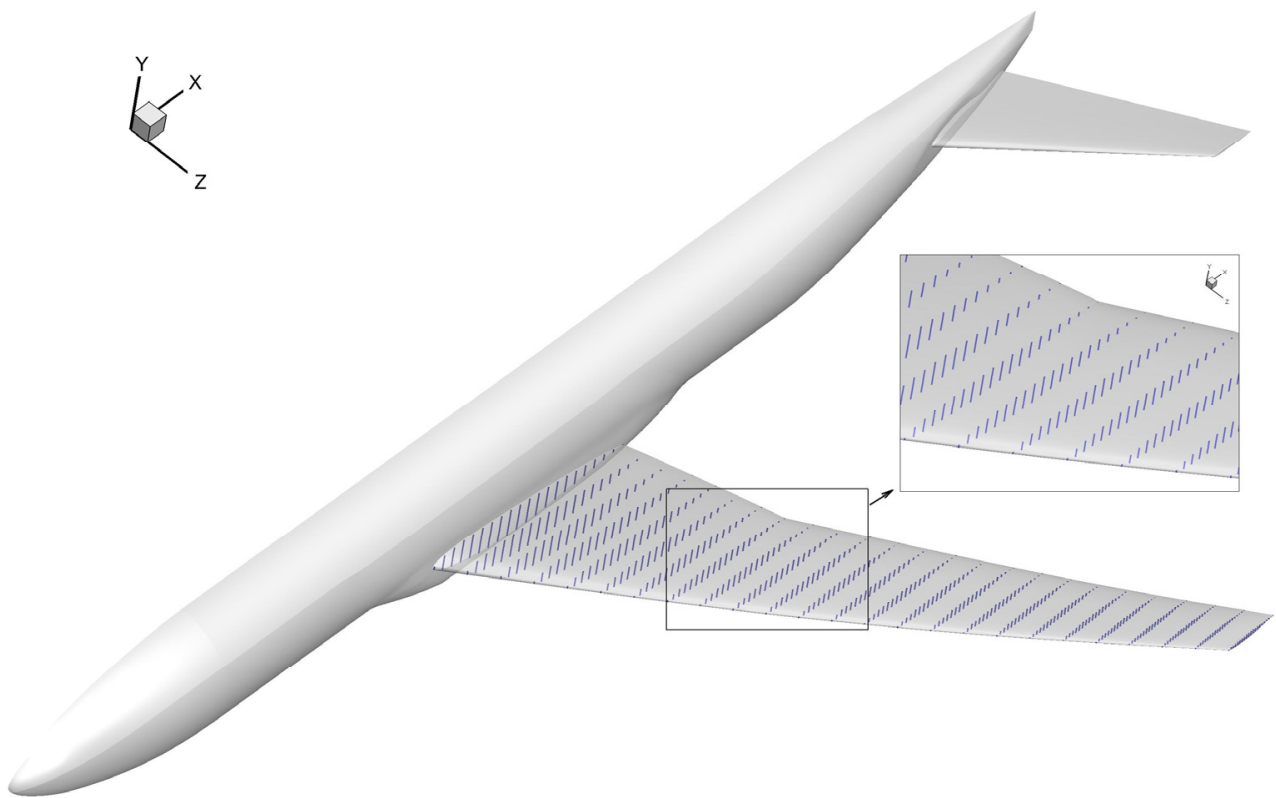


**Figure 9.** The 525 (21 chordwise  $\times$  25 spanwise) geometric constraints enforced on the wing.

Two optimization strategies are adopted in this study. The first strategy optimizes the wing–body–tail configuration without considering trimming and then manually trims the optimized configuration by deflecting the horizontal tail as a solid body. The second strategy enforces the balanced pitching moment as a constraint of the optimization, and the trimming is realized automatically by treating the tail deflection angle as a design variable. The tail rotation axis is parallel to the z-axis and is located at 40% of the tail root chord. Figure 10 shows the  $-6^\circ$  deflection of the horizontal tail relative to the original configuration. The design variables and constraints used for both strategies are listed in Table 3.

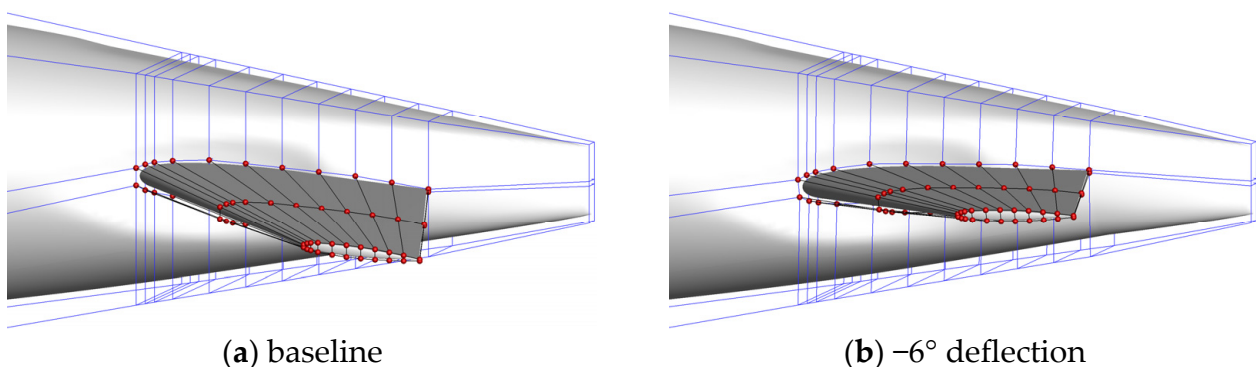


**Figure 10.** Tail deflection resulting from the deflection of a sub-FFD block.

**Table 3.** Summary of all optimization strategies.

Optimization Strategy	Design Variables		Objective	Constraints		
	Description	Quantity		Function	Description	Quantity
Strategy I	Angle of attack	1	$Min. C_D$	$C_L = 0.5$	Lift constraint	1
				$t - 0.85t_0 \geq 0$	Geometric constraints	525
	$v \geq v_0$	Volume constraint		1		
	Wing shape	80		$\Delta y_{LE}^{upper} = -\Delta y_{LE}^{lower}$	Fix the leading edge	5
				$\Delta y_{TE}^{upper} = -\Delta y_{TE}^{lower}$	Fix the trailing edge	5
Strategy II	Angle of attack	1	$Min. C_D$	$C_L = 0.5$		1
				$C_{MZ} = 0$	zero pitching moment constraint	1
	Wing shape	80		$t - 0.85t_0 \geq 0$		525
				$v \geq v_0$		1
	Tail deflection angle	1		$\Delta y_{LE}^{upper} = -\Delta y_{LE}^{lower}$		5
$\Delta y_{TE}^{upper} = -\Delta y_{TE}^{lower}$				5		

#### 4. Optimization Results

The ASO of the NASA CRM wing–body–tail configuration is performed via SBO and GBO in this section. For SBO, a multi-round optimization strategy is used to drive ASO towards the global optimum. The LHS method is used to select initial samples. EI and MSP are used to select 2 new samples, corresponding responses are solved simultaneously to update the surrogate models. For GBO, the gradient-based optimizer based on sequential quadratic programming (SQP) is used in our studies, and the gradients are provided by Adflow. All optimization works are conducted by the advanced TH-1A computing system at the National Supercomputer Center (NSCC) in Tianjin. Each computing node in this cluster has two 2.6 GHz Intel Xeon CPUs (e5-2690 V4) and 128 GB RAM in total.

##### 4.1. Strategy I: Untrimmed Optimization + Manual Trimming

This strategy optimizes the wing only and then manually trims the optimized configuration by deflecting the horizontal tail as a solid body.

Convergence histories of the objectives are shown in Figure 11. The time costs of the optimizations are listed in Table 4; we can see that SBO is more efficient than GBO for the current example with 81 design variables, since the responses of the two new samples generated by EI and MSP are solved simultaneously in each iteration of SBO. The optimal objective function value obtained via SBO is comparable to that obtained via GBO. Figure 12 shows the pressure distributions of the baseline and optimal configurations, the shock wave on the suction side is notably weakened after the optimization. The drag coefficient drops from 283.77 counts to 277.48 counts after two rounds of optimizations within the framework of SBO, which is only 0.65 counts more than that (276.83 counts) obtained via GBO.

**Table 4.** Time cost of optimization via Strategy I.

Optimization Algorithm	Computational Cost (Hours)
GBO	182.27
SBO	165.58

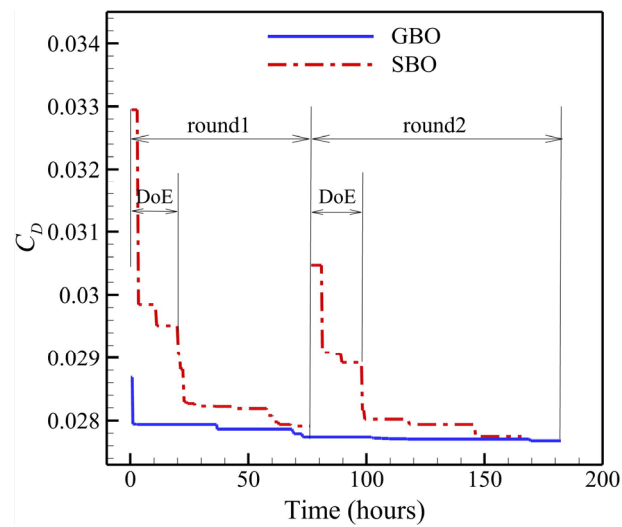


Figure 11. Convergence history of the total drag coefficient (Strategy I).

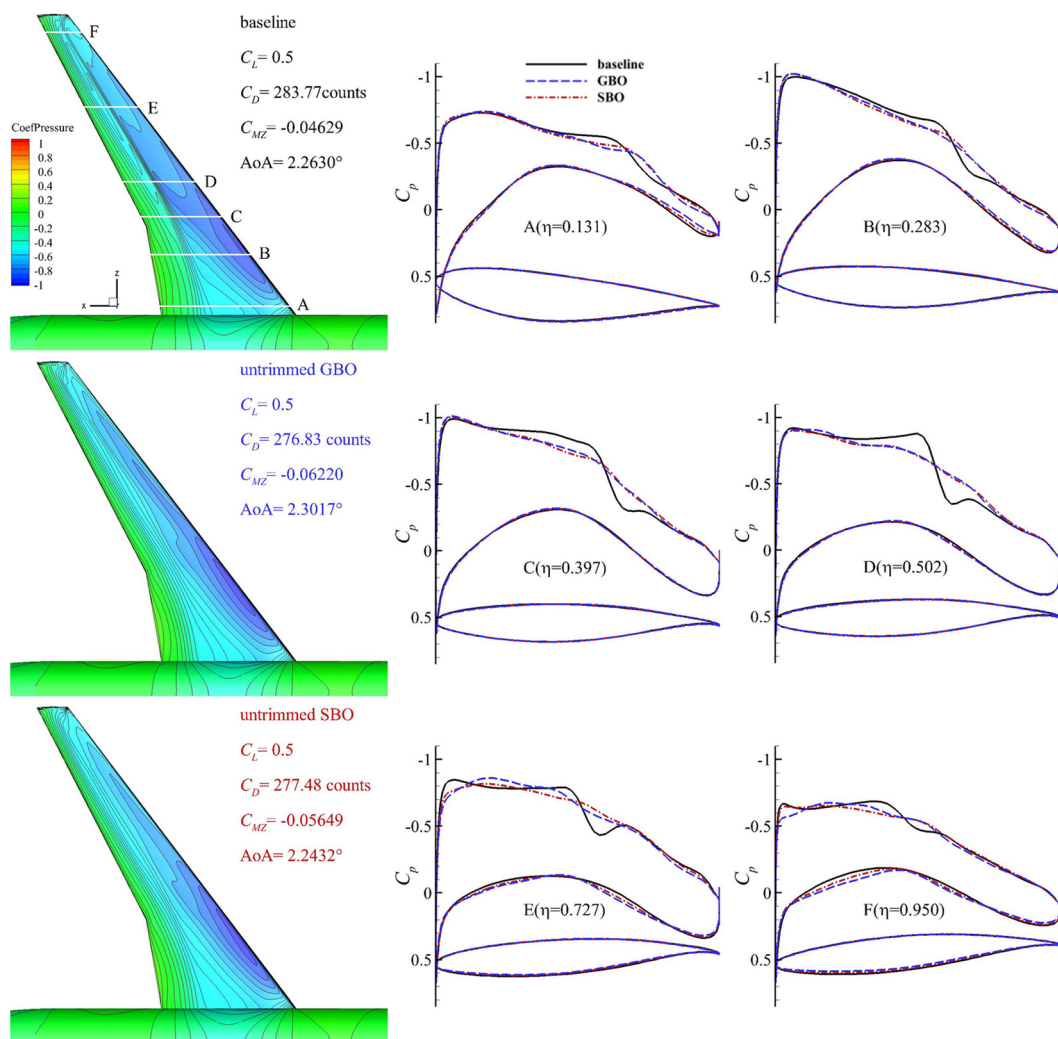
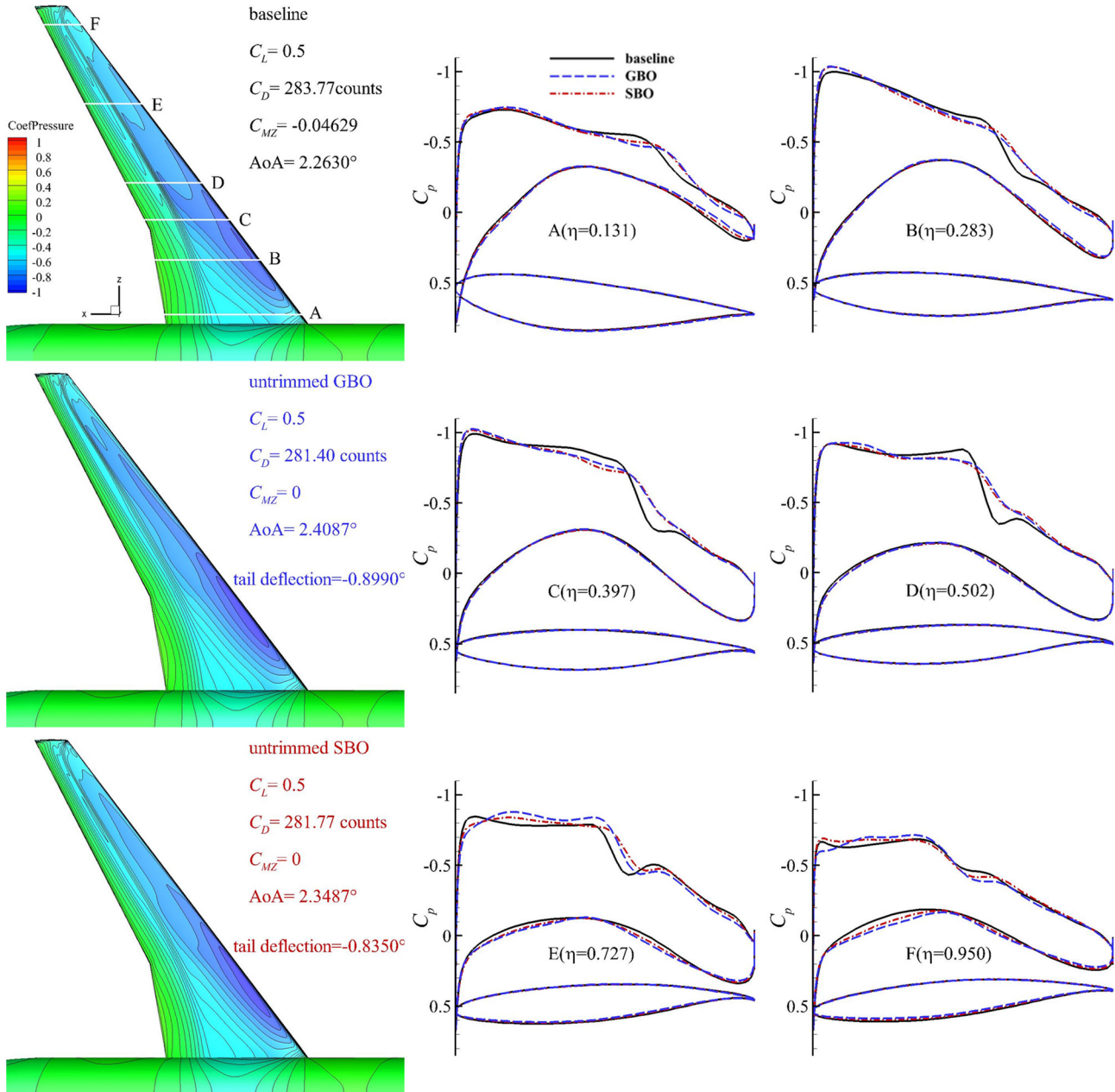


Figure 12. Comparison of pressure distributions of the baseline with untrimmed optimal configurations from Strategy I.

The optimal configurations obtained via Strategy I are then trimmed manually. Figure 13 depicts the pressure distributions of the baseline and trimmed configurations. The tail

horizontal deflection angles are  $-0.835^\circ$  and  $-0.899^\circ$  for SBO and GBO, respectively, which results in zero pitching moment coefficient for the optimal configurations, leaving the total drag coefficient at 281.77 counts and 281.4 counts due to the trim drag. The trim drag coefficient is about 4 counts.



**Figure 13.** Comparison of pressure distributions of the baseline with optimal configurations trimmed manually from Strategy I.

#### 4.2. Strategy II: Trimmed Optimization

For this strategy, the tail deflection angle is treated as a design variable to trim the aircraft, and the balanced pitching moment constraint is enforced to ensure that the pitch moment coefficient is zero.

Convergence histories of the objectives obtained via SBO and GBO are plotted in Figure 14. The time costs of the optimizations are listed in Table 5, we can see that SBO is more efficient than GBO for the design of complex aircraft configurations with 82 design variables, since the responses of the two new samples generated by EI and MSP are solved

simultaneously in each iteration of SBO. Figure 15 depicts the pressure distributions of the baseline and trimmed configurations. The shock wave on the suction side is weakened obviously after optimization. The drag coefficient drops from 283.77 counts to 278.61 counts after two rounds of optimizations within the framework of SBO, which is only 0.77 counts different from that (279.38 counts) obtained via GBO.

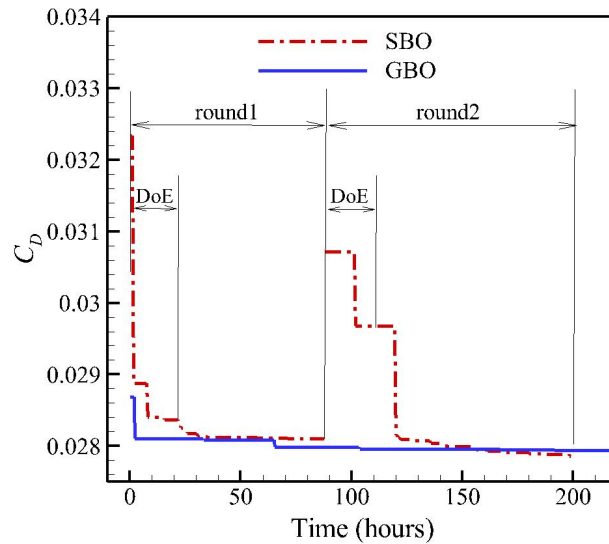


Figure 14. Convergence history of the total drag coefficient (Strategy II).

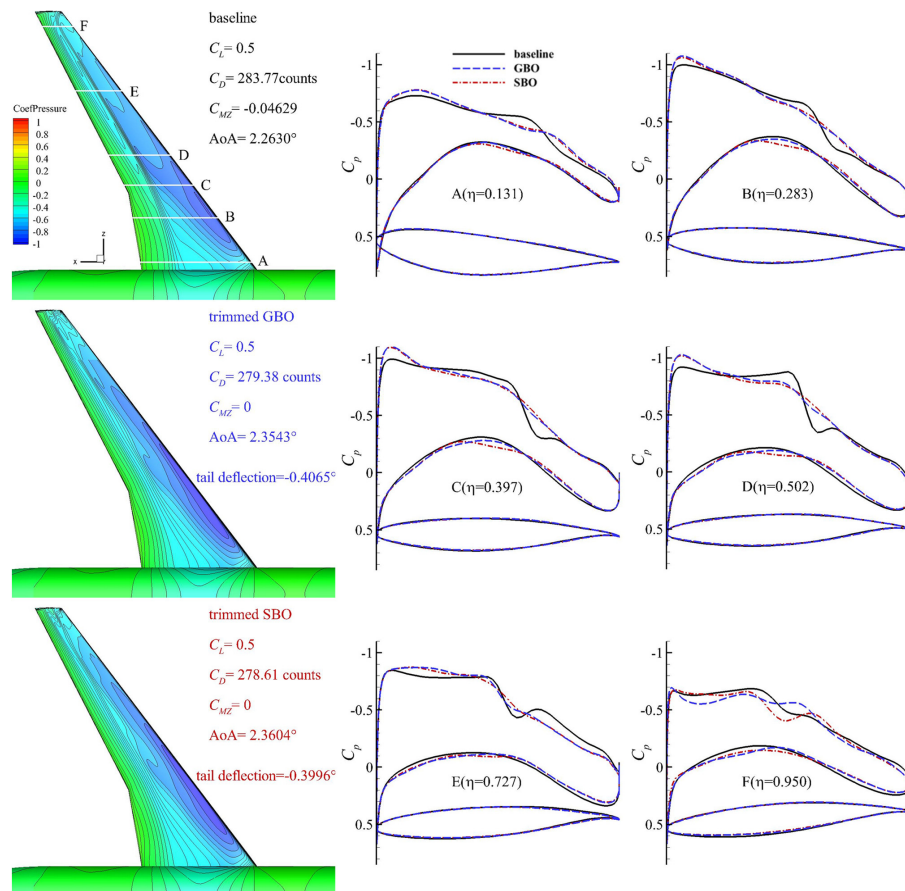


Figure 15. Comparison of pressure distributions of the baseline and optimal configurations from Strategy II.

**Table 5.** Time cost of optimization via Strategy II.

Optimization Algorithm	Computational Cost (Hours)
GBO	218.14
SBO	200.25

#### 4.3. Comparison of the Results Obtained by Using Different Optimization Strategies

The optimization results obtained by all optimization strategies are compared, as listed in Table 6. It is obvious that better optimal configurations can be obtained by considering trimming during optimization via Strategy II compared with Strategy I. A total of 3.16-drag-count drag-reducing benefits is achieved by considering trimming during optimization rather than trimming the optimized configuration manually. In addition, the optimization results obtained by GBO and SBO are compared, as listed in Table 7. One can see that the benefit of ASO achieved by SBO is comparable to that obtained by GBO, since the difference between the results obtained by these two optimization algorithms is less than 1 drag count.

**Table 6.** Comparison of the results of all optimization strategies.

Optimization Strategy	$C_L$	$C_D$ (Counts)	$C_{MZ}$	Tail Deflection Angle	Angle of Attack	
Strategy I	untrimmed	0.5	277.48	−0.05649	0°	2.2432°
	trimmed manually	0.5	281.77	0	−0.8350°	2.3487°
<b>Strategy II</b>	<b>0.5</b>	<b>278.61</b>	<b>0</b>	<b>−0.3996°</b>	<b>2.3604°</b>	

**Table 7.** Comparison of the results obtained via different optimization methods.

Optimization Method	$C_L$	$C_D$ (Counts)	$C_{MZ}$	Tail Deflection Angle	Angle of Attack	
GBO	Strategy I: trimmed manually	0.5	281.40	0	−0.8990°	2.4087°
	Strategy II	0.5	279.38	0	−0.4065°	2.3543°
SBO	Strategy I: trimmed manually	0.5	281.77	0	−0.8350°	2.3487°
	Strategy II	0.5	278.61	0	−0.3996°	2.3604°

## 5. Conclusions

In this article, the ASO of a full aircraft configuration considering trimming was investigated within the framework of a surrogate-based efficient global optimization. Two optimization strategies were adopted to optimize the NASA CRM wing–body–tail configuration. The first strategy optimizes the wing directly and then manually trims the optimized configuration by deflecting the horizontal tail. The second strategy optimizes the configuration considering trimming by adding a balanced pitching moment constraint during optimization. The optimization results are compared with those obtained via gradient-based optimization with gradients computed by the adjoint method, and the following conclusions can be drawn:

(1) Surrogate-based optimization combining the multi-round optimization strategy and Laplacian smoothing offers great potential in ASO of a full aircraft configuration. For the current test examples, it is more efficient than gradient-based optimization for design problems with around 80 design variables, and the drag reduction is comparable possibly due to the unimodal feature of the NASA CRM wing ASO [46,47]. As the number of design variables increases, gradient-based optimization becomes more efficient than surrogate-based optimization.

(2) The benefit of drag minimization can be expected to lose approximately 4 drag counts when trimming the optimal configuration obtained via untrimmed optimization.

Therefore, when optimizing the wing–body–tail configuration, it is necessary to consider the influence of the trim drag on the optimization results.

(3) Compared with the strategy that manually trims the optimal configuration obtained from an untrimmed optimization, a trimmed optimization can achieve 3.16-drag-count drag-reducing benefits by enforcing the balanced pitching moment constraint during optimization.

Beyond the scope of this article, gradient-enhanced surrogate model will be investigated for the ASO of a full aircraft configuration.

**Author Contributions:** Conceptualization, K.W. and Z.H.; methodology, K.W. and Z.H.; software, K.W. and Z.H.; validation, Z.H., K.Z. and W.S.; formal analysis, K.W.; investigation, K.W.; resources, K.W., Z.H. and W.S.; data curation, K.W.; writing—original draft preparation, K.W.; writing—review and editing, Z.H., K.Z. and W.S.; visualization, K.W.; supervision, Z.H. and K.Z.; project administration, K.W.; funding acquisition, Z.H. and K.Z. All authors have read and agreed to the published version of the manuscript.

**Funding:** This research is funded by the National Natural Science Foundation of China (grant No. U20B2007 and 11972305), as well as the Shaanxi Science Fund for Distinguished Young Scholars (grant No. 2020JC-13) and Natural Science Fund of Shaanxi Province (grant No. 2020JM-127).

**Data Availability Statement:** Not applicable.

**Conflicts of Interest:** The authors declare no conflict of interest.

## References

1. Queipo, N.V.; Haftka, R.T.; Shyy, W.; Goela, T.; Vaidyanathan, R.; Tucker, P.K. Surrogate-based analysis and optimization. *Prog. Aerosp. Sci.* **2005**, *45*, 1–28. [[CrossRef](#)]
2. Forrester, A.I.J.; Keane, A.J. Recent advances in surrogate-based optimization. *Prog. Aerosp. Sci.* **2009**, *45*, 50–79. [[CrossRef](#)]
3. Haftka, R.T.; Villanueva, D.; Chaudhuri, A. Parallel surrogate-assisted global optimization with expensive functions—a survey. *Struct. Multidiscip. Optim.* **2016**, *54*, 3–13. [[CrossRef](#)]
4. Parr, J.M.; Keane, A.J.; Forrester, A.I.J.; Holden, C.M.E. Infill sampling criteria for surrogate-based optimization with constraint handling. *Eng. Optimiz.* **2012**, *44*, 1147–1166. [[CrossRef](#)]
5. Han, Z.H. Kriging surrogate model and its application to design optimization: A review of recent progress. *Acta Aeronaut. Astronaut. Sin.* **2016**, *37*, 3197–3225. (In Chinese)
6. Viana, F.A.C.; Simpson, T.W.; Balabanov, V.; Toropov, V. Metamodeling in multidisciplinary design optimization: How far have we really come? *AIAA J.* **2014**, *52*, 670–690. [[CrossRef](#)]
7. Han, Z.H.; Goertz, S.; Zimmermann, R. Improving variable-fidelity surrogate modeling via gradient enhanced Kriging and a generalized hybrid bridge function. *Aerosp. Sci. Tech.* **2013**, *25*, 177–189. [[CrossRef](#)]
8. Han, Z.H. SurroOpt: A generic surrogate-based optimization code for aerodynamic and multidisciplinary design. In Proceedings of the ICAS 2016, Daejeon, Republic of Korea, 25–30 September 2016.
9. Liu, J.; Song, W.P.; Han, Z.H.; Zhang, Y. Efficient aerodynamic shape optimization of transonic wings using a parallel infilling strategy and surrogate models. *Struct. Multidiscip. Optim.* **2017**, *55*, 925–943. [[CrossRef](#)]
10. Han, Z.H.; Xu, C.Z.; Zhang, L.; Zhang, Y.; Zhang, K.S.; Song, W.P. Efficient aerodynamic shape optimization using variable-fidelity surrogate models and multilevel computational grids. *Chin. J. Aeronaut.* **2020**, *33*, 31–47. [[CrossRef](#)]
11. Courrier, N.; Boucard, P.A.; Soulier, B. Variable-fidelity modeling of structural analysis of assemblies. *J. Global. Optim.* **2016**, *64*, 577–613. [[CrossRef](#)]
12. Ha, H.; Oh, S.; Yee, K. Feasibility study of hierarchical kriging model in the design optimization process. *J. Korean Soc. Aero. Spac. Sci.* **2014**, *42*, 108–118. [[CrossRef](#)]
13. Jo, Y.; Choi, S.; Lee, D.J.; Choi, D.Z. Adaptive variable-fidelity analysis and design using dynamic fidelity indicators. *AIAA J.* **2016**, *54*, 3564–3579. [[CrossRef](#)]
14. Leifsson, L.; Koziel, S. Aerodynamic shape optimization by variable-fidelity computational fluid dynamics models: A review of recent progress. *J. Comput. Sci.* **2015**, *10*, 45–54. [[CrossRef](#)]
15. Leifsson, L.; Koziel, S.; Tesfahunegn, Y.A. Multiobjective aerodynamic optimization by variable-fidelity models and response surface surrogate models. *AIAA J.* **2016**, *54*, 531–541. [[CrossRef](#)]
16. Zhang, Y.; Han, Z.H.; Zhang, K.S. Variable-fidelity expected improvement for efficient global optimization of expensive functions. *Struct. Multidiscip. Optim.* **2018**, *58*, 1431–1451. [[CrossRef](#)]
17. Han, Z.H.; Zhang, Y.; Song, C.X.; Zhang, K.S. Weighted gradient-enhanced kriging for high-dimensional surrogate modeling and design optimization. *AIAA J.* **2017**, *55*, 4330–4346. [[CrossRef](#)]
18. Laurenceau, J.; Meaux, M.; Montagnac, M.; Sagaut, P. Comparison of gradient-based and gradient-enhanced response-surface-based optimizers. *AIAA J.* **2012**, *48*, 981–994. [[CrossRef](#)]

19. Mortished, C.; Ollar, J.; Jones, R.; Benzie, P.; Toropov, V.; Sienz, J. Aircraft wing optimization based on computationally efficient gradient-enhanced Kriging. In Proceedings of the 57th AIAA/ASCE/AHS/ASC Structures, Structural Dynamics, and Materials Conference, San Diego, CA, USA, 4–8 January 2016.
20. Bouhlel, M.A.; Martins, J.R.R.A. Gradient-enhanced kriging for high-dimensional problems. *Eng. Comput. Ger.* **2019**, *35*, 157–173. [[CrossRef](#)]
21. Li, J.C.; Zhang, M. Adjoint-free Aerodynamic Shape Optimization of the Common Research Model Wing. *AIAA J.* **2021**, *59*, 1990–2000. [[CrossRef](#)]
22. Li, J.C.; Cai, J.S.; Qu, K. Surrogate-based aerodynamic shape optimization with the active subspace method. *Struct. Multidiscip. Optim.* **2019**, *59*, 403–419. [[CrossRef](#)]
23. Bouhlel, M.A.; Bartoli, N.; Regis, R.G.; Otsmane, A.; Morlier, J. Efficient global optimization for high-dimensional constrained problems by using the Kriging models combined with the partial least squares method. *Eng. Optimiz.* **2018**, *50*, 2038–2053. [[CrossRef](#)]
24. Zhang, K.S.; Han, Z.H.; Gao, Z.J.; Wang, Y. Constraint aggregation for large number of constraints in wing surrogate-based optimization. *Struct. Multidiscip. Optim.* **2019**, *59*, 421–438. [[CrossRef](#)]
25. Wang, K.; Han, Z.H.; Zhang, K.S.; Song, W.P. An Efficient Geometric Constraint Handling Method for Surrogate-Based Aerodynamic Shape Optimization. *Eng. Appl. Comp. Fluid* **2023**, *17*, e2153173. [[CrossRef](#)]
26. Zhang, Y.; Han, Z.H.; Shi, L.X.; Song, W.P. Multi-round Surrogate-based Optimization for Benchmark Aerodynamic Design Problems. In Proceedings of the 54th AIAA Aerospace Sciences Meeting, San Diego, CA, USA, 4–8 January 2016.
27. Li, J.C.; Zhang, M. Drag Reduction of Transonic Wings with Surrogate-Based Optimization. In Proceedings of the 2018 Asia-Pacific International Symposium on Aerospace Technology, Chengdu, China, 15–19 October 2018.
28. Han, Z.H.; Zhang, Y.; Xu, C.Z.; Wang, K.; Wu, M.M.; Zhu, Z.; Song, W.P. Aerodynamic optimization design of large civil aircraft wings using surrogate-based model. *Acta Aeronaut. Astronaut. Sin.* **2019**, *40*, 522398. (In Chinese)
29. Chen, S.; Lyu, Z.J.; Kenway, G.K.W.; Martins, J.R.R.A. Aerodynamic shape optimization of common research model wing-body-tail configuration. *J. Aircr.* **2016**, *53*, 276–293. [[CrossRef](#)]
30. Lyu, Z.J.; Martins, J.R.R.A. Aerodynamic design optimization studies of a blended-wing-body aircraft. *J. Aircr.* **2014**, *51*, 1604–1617. [[CrossRef](#)]
31. Koo, D.; Zingg, D.W. Progress in Aerodynamic Shape Optimization Based on the Reynolds-Averaged Navier-Stokes Equations. In Proceedings of the 54th AIAA Aerospace Sciences Meeting, San Diego, CA, USA, 4–8 January 2016.
32. Merle, A.; Stück, D.W.; Rempke, A. An Adjoint-based Aerodynamic Shape Optimization Strategy for Trimmed Aircraft with Active Engines. In Proceedings of the 35th AIAA Applied Aerodynamics Conference, Denver, CO, USA, 5–9 June 2017.
33. Kenway, G.K.W.; Secco, N.; Martins, J.R.R.A.; Mishra, A.; Duraisamy, K. An Efficient Parallel Overset Method for Aerodynamic Shape Optimization. In Proceedings of the 58th AIAA/ASCE/AHS/ASC Structures, Structural Dynamics, and Materials Conference, Grapevine, TX, USA, 9–13 January 2017.
34. Lei, R.W.; Bai, J.Q.; Xu, D.Y. Aerodynamic optimization of civil aircraft with wing-mounted engine jet based on adjoint method. *Aerosp. Sci. Tech.* **2019**, *93*, 105285. [[CrossRef](#)]
35. Sederberg, T.W.; Parry, S.R. Free-form deformation of solid geometric models. *ACM Siggraph Comput. Graph.* **1986**, *20*, 151–160. [[CrossRef](#)]
36. Giunta, A.A.; Wojtkiewicz, J.S.F.; Eldred, M.S. Overview of Modern Design of Experiments Methods for Computational Simulations. In Proceedings of the 41st AIAA Aerospace Sciences Meeting and Exhibit, Reno, NV, USA, 6–9 January 2003.
37. Mader, C.A.; Kenway, G.K.W.; Yildirim, A.; Martins, J.R.R.A. ADflow: An Open-Source Computational Fluid Dynamics Solver for Aerodynamic and Multidisciplinary Optimization. *J. Aerosp. Inf. Syst.* **2020**, *17*, 508–527. [[CrossRef](#)]
38. Jameson, A.; Schmidt, W.; Turkel, E. Numerical Solution of the Euler Equations by Finite Volume Methods Using Runge–Kutta Time Stepping Schemes. In Proceedings of the 14th Fluid and Plasma Dynamics Conference, Palo Alto, CA, USA, 23–25 June 1981.
39. Klopfer, G.; Hung, C.; Wijngaart, R.V.D.; Onufer, J. A diagonalized diagonal dominant alternating direction implicit (D3ADI) scheme and subiteration correction. In Proceedings of the 29th AIAA, Fluid Dynamics Conference, Albuquerque, NM, USA, 15–18 June 1998.
40. Saad, Y.; Schultz, M.H. GMRES: A Generalized Minimal Residual Algorithm for Solving Nonsymmetric Linear Systems. *Siam J. Sci. Comput.* **1986**, *7*, 856–869. [[CrossRef](#)]
41. Balay, S.; Brown, J.; Buschelman, K.; Eijkhout, V.; Gropp, W.D.; Kaushik, D.; Knepley, M.G.; McInnes, L.C.; Smith, B.F.; Zhang, H. *PETSc Users Manual, Technical Report ANL-95/11—Revision 3.4*; Argonne National Laboratory: Lemont, IL, USA, 2013.
42. Han, Z.H.; Chen, J.; Zhang, K.S.; Xu, Z.M.; Zhu, Z.; Song, W.P. Aerodynamic Shape Optimization of Natural-Laminar-Flow Wing Using Surrogate-Based Approach. *AIAA J.* **2018**, *56*, 2579–2593. [[CrossRef](#)]
43. Bu, Y.P.; Song, W.P.; Han, Z.H.; Zhang, Y.; Zhang, L. Aerodynamic/aeroacoustic variable-fidelity optimization of helicopter rotor based on hierarchical Kriging model. *Chin. J. Aeronaut.* **2020**, *33*, 476–492. [[CrossRef](#)]
44. Han, Z.H.; Xu, C.Z.; Qiao, J.L.; Liu, F.; Chi, J.B.; Meng, G.Y.; Zhang, K.S.; Song, W.P. Recent progress of efficient global aerodynamic shape optimization using surrogate-based approach. *Acta Aeronaut. Astronaut. Sin.* **2020**, *41*, 623344. (In Chinese)
45. Kreisselmeier, G.; Steinhauser, R. Systematic control design by optimizing a vector performance index. In Proceedings of the IFAC Symposium on computer Aided Design of Control Systems, Zurich, Switzerland, 29–31 August 1979.

46. He, X.L. Multi-Component Adaptive Aerodynamic Shape Optimization Methods for Civil Transport Aircrafts. Ph.D. Thesis, Northwestern Polytechnical University, Wuhan, China, 2019. (In Chinese).
47. Yu, L.; Lyu, Z.J.; Xu, Z.L.; Martins, J.R.R.A. On the influence of optimization algorithm and initial design on wing aerodynamic shape optimization. *Aerosp. Sci. Tech.* **2018**, *75*, 183–199. [[CrossRef](#)]

**Disclaimer/Publisher’s Note:** The statements, opinions and data contained in all publications are solely those of the individual author(s) and contributor(s) and not of MDPI and/or the editor(s). MDPI and/or the editor(s) disclaim responsibility for any injury to people or property resulting from any ideas, methods, instructions or products referred to in the content.